nature communications

Article

https://doi.org/10.1038/s41467-025-62622-z

Metal-driven anaerobic oxidation of methane and the Sturtian deglaciation

Received: 29 October 2024

Accepted: 28 July 2025

Published online: 06 August 2025

Check for updates

Jun Hu[1,2], Sanzhong Li[1,2] ✉, Shui-Jiong Wang[3,4] ✉, Jörn Peckmann[5], Hongxiang Guan[1,2], Shao-yong Jiang[6], Wei Chen[6], Huan Cui[7], Zheng Qin[3], Peng Liu[1,2], Yanhui Suo[1,2], Zhaoxia Jiang[1,2], Dongyong Li[1,2], Nan Wang[1,2], Xiaohui Li[1,2], Yuan Zhong[1,2], Ruru Li[1], Xi-Ming Yang[3] & Kurt O. Konhauser[8]

The Sturtian and Marinoan glaciations shaped Neoproterozoic palaeoenvironmental evolution. While methane emission likely intensified the Marinoan greenhouse effect, its role during the Sturtian glaciation—coinciding with widespread iron formations (IFs)—remains poorly understood. Here, we analysed bio-essential metals (Ni, Co, Zn), rare earth elements and yttrium (REY), Fe (δ^{56}Fe) and Ni (δ^{60}Ni) isotopes in hematite and magnetite, alongside bulk-rock and in-situ C isotopes of Mn-rich carbonates from five well-preserved Sturtian-aged IFs in South China. Our findings provide geochemical evidence for a methane-related biogeochemical pathway driving Fe-bearing mineral transformation via methanogenesis and metal-driven anaerobic methane oxidation (AOM), mediated by methanogens and anaerobic methane-oxidizing archaea (ANME) in ferruginous settings. Additionally, the Sturtian deglaciation facilitated atmospheric-oceanic O_2 exchange, increased nutrient influx from weathering, and methane release under slow AOM oxidation kinetics, potentially aiding ice sheet melting or prolonging glacial waning.

The Cryogenian Period, spanning the Sturtian (ca. 717–660 Ma) and Marinoan (ca. 650–635 Ma) Snowball Earth glaciations, includes a 10-million-year interglacial interval termed the Cryogenian non-glacial interlude (ca. 660–650 Ma)[1–3]. These two global glaciations and their associated extreme climate fluctuations likely had drastic effects on the evolution of the Earth's palaeoenvironment-life system[3–7]. Notably, the recession of glaciers was particularly associated with enhanced continental weathering, increased riverine supply of nutrients, including dissolved phosphate (PO_4^{3-}) and sulfate (SO_4^{2-}), and recovery of marine productivity[6,7]. This transition from icehouse to greenhouse climatic conditions was likely pivotal for subsequent periods of rapid biological innovation, including the shift from a prokaryote-dominated to a eukaryote-dominated biological marine phytoplankton and the prominent rise of complex multicellular eukaryotes[6–9]. This climatic shift has traditionally been attributed to the long-term build-up of an exceptionally high atmospheric carbon dioxide (CO_2) concentration, estimated to have reached about 350 times the present atmospheric level (PAL), leading to rapid melting of Earth's ice sheets[10]. Geochemical data also indicate that active methanogenesis and significant methane (CH_4) emissions further intensified the greenhouse effect during the Marinoan deglaciation[5,11,12]. Methane is a potent greenhouse gas with a global warming potential > 27 times that of CO_2, playing a crucial role in the global carbon (C) cycle[13]. Nevertheless, the role of CH_4

[1]Frontiers Science Center for Deep Ocean Multispheres and Earth System, Key Lab of Submarine Geosciences and Prospecting Techniques, MOE and College of Marine Geosciences, Ocean University of China, Qingdao, China. [2]Laoshan Laboratory, Laboratory for Marine Mineral Resources, Qingdao Marine Science and Technology Center, Qingdao, China. [3]State Key Laboratory of Geological Processes and Mineral Resources, China University of Geosciences (Beijing), Beijing, China. [4]Frontiers Science Center for Deep-time Digital Earth, China University of Geosciences (Beijing), Beijing, China. [5]Fachbereich Erdsystemwissenschaften, Universität Hamburg, Hamburg, Germany. [6]State Key Laboratory of Geological Processes and Mineral Resources, School of Earth Resources, China University of Geosciences, Wuhan, China. [7]Department of Geology, Kansas State University, Manhattan, KS, USA. [8]Department of Earth and Atmospheric Sciences, University of Alberta, Edmonton, AB, Canada. ✉e-mail: sanzhong@ouc.edu.cn; wsj@cugb.edu.cn

and its connection to marine biogeochemical cycles during the Sturtian glaciation remains largely unexplored.

The Sturtian glaciation, the first and longest of the Cryogenian ice ages (ca. 57 My), is also characterized by the resurgence of iron formations (IFs)[1,4,14,15]. This sudden and conspicuous global reappearance of Sturtian-aged IF deposition, following a nearly 1-billion-year hiatus in the sedimentary record, indicates anoxic deep waters enriched in dissolved Fe^{2+} [3,4,14]. The formation of Sturtian-aged IFs is closely linked to the evolution of glacial systems[4,16]. These IFs are pivotal in deciphering the Cryogenian ocean chemistry and glacial climate dynamics[17]. For instance, Sturtian-aged IFs in northern Namibia, south Australia, and California were deposited across a range of glaciomarine environments, from ice-contact to ice-distal settings under sea ice cover[4,17,18]. However, Sturtian-aged IFs in the Nanhua Basin of the South China Block (SCB) (Fig. 1a) exhibit distinct depositional environments and are thought to have formed during the waning stage of the Sturtian glaciation, exhibiting minimal glacial influence[16,19–21] (Fig. 1b; Supplementary Fig. 1; Supplementary Information).

IFs are marine chemical sediments rich in iron (Fe), predominantly composed of Fe^{3+}- and Fe^{2+}-bearing minerals such as hematite, magnetite, and Fe-rich carbonates (e.g., ankerite and siderite)[22,23]. These Fe-bearing minerals are generally interpreted as originating from Fe^{3+} oxyhydroxide ($Fe(OH)_3$) precursors[22,23]. Their formation is attributed to multiple Fe^{2+} oxidation pathways, including reaction with molecular oxygen (O_2) from oxygenic photosynthesis, photoferrotrophy, and microaerophilic chemolithoautotrophic bacterial oxidation[22,24]. Hematite is interpreted to have formed either via direct dehydration of a precursor $Fe(OH)_3$ phase during diagenesis or fluid-mediated oxidation and replacement of an Fe^{2+} phase[25]. Transformation of $Fe(OH)_3$ precursors at IF deposition sites also drives diagenetic processes that produce magnetite and Fe^{2+}-rich carbonates, which are closely linked to the biogeochemical cycling of Fe and C in anoxic environments[26–29]. It is widely accepted that such Fe-bearing mineral transformations were predominantly driven by microbial dissimilatory iron reduction (DIR), wherein $Fe(OH)_3$ reduction was coupled to the oxidation of organic matter, with Fe^{3+} serving as the terminal electron acceptor[22,24,26,28–30]. However, Konhauser et al.[26] proposed Fe^{3+} reduction might have also been linked to anaerobic oxidation of CH_4 (AOM) in anoxic marine sediments.

In the present-day environment, most AOM is sulfate-dependent[31,32]. Such a process may not have been efficient during the Precambrian, owing to low SO_4^{2-} concentrations[33]. In recent years, AOM coupled with the reduction of Fe $(OH)_3$ and Mn oxides (MnO_2) has emerged as a globally significant biogeochemical process in O_2-depleted environments[34–38]. Indeed, metal-dependent AOM, where $Fe(OH)_3$ and MnO_2 act as electron acceptors, likely played a prevalent role in Precambrian oceans given that much of the global oceans remained ferruginous until at least the early Palaeozoic[38–42]. These conditions, characterized by high dissolved Fe^{2+} in porewater, minimal SO_4^{2-}, elevated CH_4 concentrations, and abundant reactive $Fe(OH)_3$ and MnO_2, provide a conducive geochemical setting for metal-dependent AOM[33–35,43]. Despite its significance, the exact mechanisms of this CH_4-related process in the Precambrian remain poorly understood.

In this study, we examined five well-preserved Sturtian-aged IFs in the SCB (Fig. 1a, b), which host diverse Fe-rich and manganese (Mn)-rich minerals, including hematite, magnetite, ankerite, manganosiderite, and occasionally pyrite (Supplementary Figs. 2, 3). This mineralogical diversity provides a unique opportunity to explore direct evidence of CH_4-driven processes. The formation of these minerals associated with CH_4 cycling may yield distinct patterns in metal element distributions and isotopic compositions[5,42,44,45]. These patterns reflect microbial metabolic variability and interactions with trace nutrients or metalloenzymes[5,42,45,46]. Methanogens and anaerobic methane-oxidizing archaea (ANME), which mediate these processes, rely on metal cofactors, such as nickel (Ni), cobalt (Co), and zinc (Zn), for electron transport and catalysis[44,45,47]. Furthermore, these microbes can preferentially incorporate isotopically light Ni and selectively accumulate heavy rare earth elements (HREE)[5,45,48,49]. These distinct biogeochemical signatures may ultimately be concentrated within authigenic Fe-bearing minerals[5,45].

We analysed Ni and Fe isotopes, along with bio-essential metals (Ni, Co, and Zn), and REE and yttrium (REY) in hematite and magnetite, as well as the bulk and in-situ C isotopic composition of Mn-rich carbonates. These geochemical proxies hold promise for elucidating the role of CH_4 and its connection to the palaeoenvironment-life system during the waning stage of the Sturtian glaciation.

Results

Geological setting and sample description

The Sturtian and Marinoan glacial deposits, along with the notably warm interglacial interval, are well-preserved in the Nanhua Basin of the Yangtze Block[3] (Fig. 1b; Supplementary Fig. 1). The Cryogenian stratigraphy of the Nanhua Basin, with well-constrained global chronologies, consists of the Chang'an, Fulu, Datangpo, and Nantuo formations in ascending order, along with their correlative equivalents in the slope-to-basin environment[50] (Fig. 1a; Supplementary Fig. 1). The Sturtian glacial deposits are represented by the Chang'an and Fulu formations, while the Nantuo Formation corresponds to the Marinoan glaciation, with the non-glacial, Mn-rich Datangpo Formation separating them[3,6] (Fig. 1b; Supplementary Fig. 1).

The Sturtian glacial deposits in the Nanhua Basin comprise multiple diamictite–sandstone/siltstone cycles, likely reflecting dynamic ice sheet fluctuations[19,21] (SI). The Chang'an Formation, dominated by massive and stratified diamictites, represents the main waxing phase of the Sturtian glaciation and glacier advance[19,21] (Fig. 1b; Supplementary Fig. 1). The overlying Fulu Formation is stratigraphically subdivided into two distinct lithological members (Fig. 1b; Supplementary Fig. 1). The basal member primarily comprises sandstones and muddy siltstones, with occasional dolostone intercalations. Sedimentary structures, lithological characteristics, and geochemical proxies indicate a depositional environment with minimal direct glacial influence (SI). This succession is interpreted as representing the waning stage of the Sturtian glaciation, marking the progression of deglaciation[2,19–21,51] (Fig. 1b; Supplementary Fig. 1). The upper member of the Fulu Formation is characterized by the reappearance of massive and crudely stratified diamictites, indicating a glacial re-advance. This assemblage is interpreted as recording the second waxing phase of the Sturtian glaciation[2,19–21,51] (Fig. 1b; Supplementary Fig. 1).

The Sturtian-aged IFs of the Nanhua Basin occur at the base of the first member of the Fulu Formation, conformably overlying the diamictites of the Chang'an Formation (Fig. 1b; Supplementary Fig. 1). These IFs are stratigraphically correlated across the slope-to-basin environment, exhibiting distinct palaeoenvironmental and palaeogeographic patterns[52,53] (Fig. 1a, b; SI). Palaeoenvironmentally, the Tongdao and Xinyu IFs were deposited within a broad slope-to-basin environment, whereas the Sanjiang, Jiangkou, and Qidong IFs were formed in an inferred deep-water sub-basin delineated within this broader setting, indicative of relatively deeper depositional conditions[8,21,51,53,54] (Fig. 1a; SI). Palaeogeographically, the Xinyu IF was positioned nearest to the oldland, while the Tongdao IF formed on a submarine uplift developed atop a pre-existing structural high, as indicated by isopach patterns of the local Fulu Formation[8,21,51,53,54] (Fig. 1a). While the current palaeogeographic reconstruction provides a valuable spatial framework (Fig. 1a), it remains provisional due to limited stratigraphic resolution, incomplete exposure of the Cryogenian strata in certain areas, and the tectonic complexity of the SCB (SI). Critically, these uncertainties do not compromise the sampling strategy and the interpretation of the geochemical data, which are central to this study.

https://doi.org/10.1038/s41467-025-62622-z

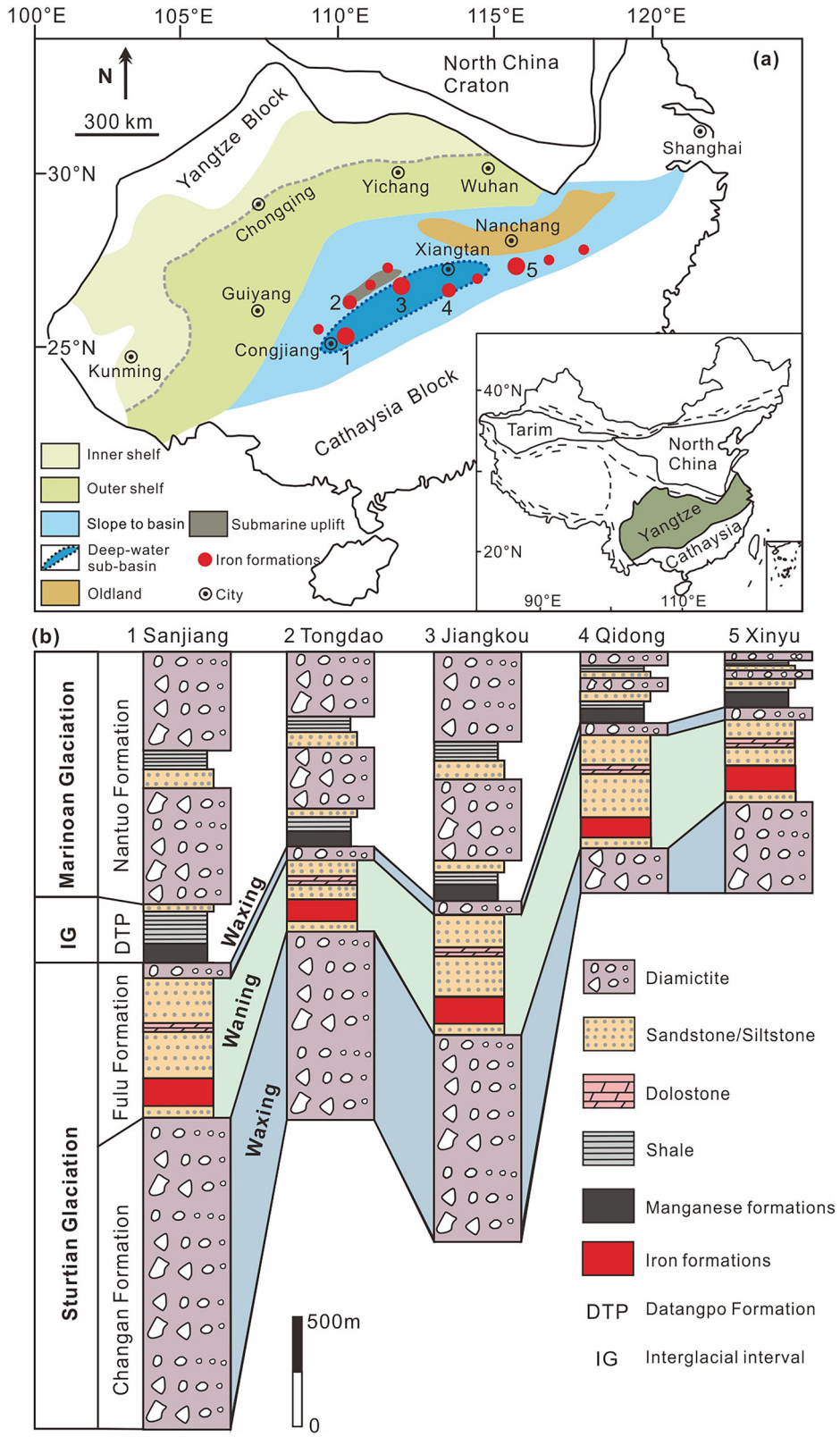

These five studied IFs are interlayered with sandstones and siltstones (Fig. 1b) and have experienced localized low-greenschist facies metamorphism into slate and phyllite[52,53]. Notably, these IFs lack glacial indicators such as diamictites, faceted or striated clasts, and ice-rafted dropstones within their successions. The absence of clear glacial influence suggests their formation during the waning phase between two Sturtian glacial episodes[2,16,19–21] (Fig. 1b; Supplementary Fig. 1). This study focuses on distinctly banded IF lithologies, with banding evident in both hand specimens and microscopic observations (Supplementary Figs. 2, 3). Mineralogically, the Sanjiang IF is primarily composed of hematite and quartz (Supplementary Fig. 2a, b). In contrast, the other four IFs (Tongdao, Jiangkou, Qidong, and Xinyu) contain both hematite and magnetite. The proportion of magnetite progressively decreases from the Xinyu IF, through the Tongdao IF, to the Jiangkou

https://doi.org/10.1038/s41467-025-62622-z

Fig. 1 | Palaeogeographic setting and stratigraphic correlation of Sturtian iron formations in the South China Block. a Palaeogeographic reconstruction of the South China Block (SCB) during the late Neoproterozoic Era, showing the distribution of Sturtian-aged iron formations (IFs) in the region[5,8,21,51,52,54,106]; 1 (Sanjiang IF); 2 (Tongdao IF); 3 (Jiangkou IF); 4 (Qidong IF); and 5 (Xinyu IF). The inset shows the geographic locality of the Yangtze Block. The shelf is subdivided into inner and outer regions. Within the broader slope-to-basin environment, an inferred deep-water sub-basin is delineated, reflecting relatively greater water depth (Supplementary Information). This palaeogeographic framework is primarily informed by previous regional interpretations, including stratigraphic, sedimentological, and lithofacies features, and remains provisional in nature (see main text and SI for a detailed discussion of its limitations). Symbols for IFs and submarine uplifts are not to scale and are exaggerated for illustrative purposes. **b** Representative stratigraphic columns illustrating the correlation of the studied IFs with the waxing and waning cycles of the Sturtian glaciation in the SCB[5,8,19,21,51–53]. The thicknesses of the IFs, manganese formations, and intervening dolostone layers in the Fulu Formation, as well as the pebble-free siltstone, sandstone, and shale layers in the Nantuo Formation, are exaggerated for illustrative purposes and do not accurately represent their true dimensions.

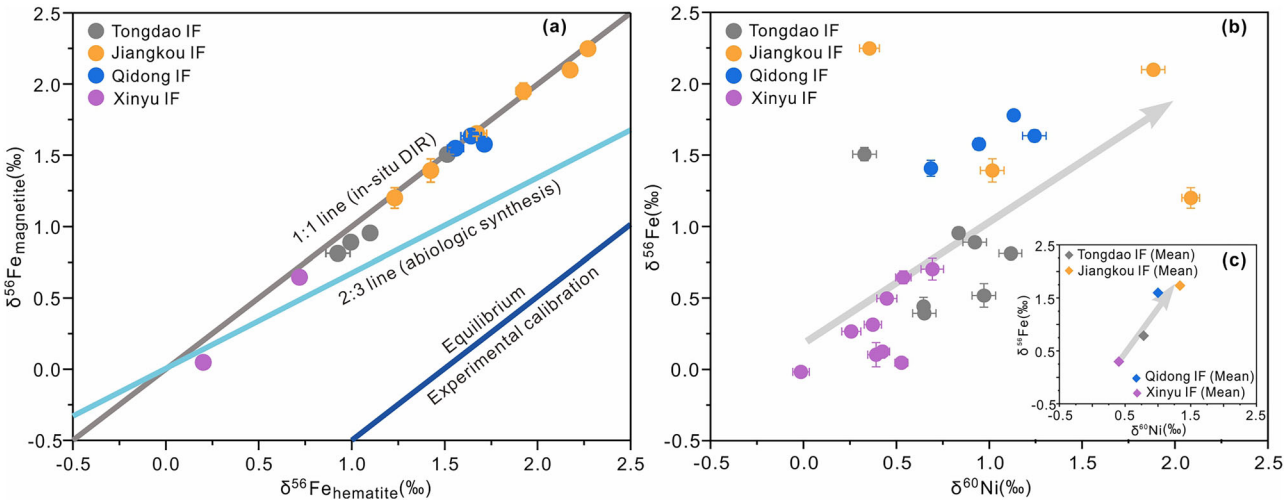

Fig. 2 | Fe and Ni isotope systematics in magnetite and hematite from the studied Sturtian iron formations. a Variations in Fe isotope compositions between coexisting hematite and magnetite, highlighting distinct trends that delineate diverse pathways of magnetite formation[30]. The Fe isotope fractionations for equilibrium hematite and magnetite formation are illustrated in blue[30,107]. The gray line labeled "1:1" represents the origin of magnetite through the in-situ dissimilatory iron reduction (DIR) of the common precursor $Fe(OH)_3$[22,27]. **b**, **c** Cross-plots of $\delta^{60}Ni$ versus $\delta^{56}Fe$ values for magnetite samples. Plot (**c**) displays average $\delta^{60}Ni$ and $\delta^{56}Fe$ values. The $\delta^{60}Ni$ and $\delta^{56}Fe$ values of magnetite exhibit a positive correlation. Error bars for the $\delta^{56}Fe$ and $\delta^{60}Ni$ data represent two standard deviations (2 SD).

and Qidong IFs (Supplementary Figs. 2, 3). Additionally, the four magnetite-containing IFs all contain Mn-rich carbonates, aluminosilicates and apatite (Supplementary Figs. 2, 3). Pyrite is predominantly observed in the Xinyu IF (Supplementary Fig. 3g, i, k). A detailed description of petrological characteristics is provided in the Supplementary Information.

Ni, Fe and C isotopic data

Magnetite from the Tongdao, Jiangkou, Qidong, and Xinyu IFs exhibits a wide range of Ni isotopic compositions, with $\delta^{60}Ni$ values varying from −0.01‰ to 2.09‰, predominantly falling within the range of −0.01‰ to 1.24‰ (Figs. 2b and 5d; Supplementary Data 1). A similar variability is observed in $\delta^{56}Fe$ values across all selected hematite and magnetite samples, with values ranging from 0.20 to 2.27‰ and −0.20 to 2.25‰, respectively (Figs. 2a and 5e; Supplementary Fig. 7c; Supplementary Data 2). Furthermore, the $\delta^{56}Fe$ values of coexisting hematite and magnetite pairs from fifteen IF samples exhibit remarkable consistency, with a difference less than 0.15‰, demonstrating a clear linear correlation (Fig. 2a). Bulk-rock $\delta^{13}C_{V\text{-}PDB}$ values from the IFs range between −13.2‰ and −6.7‰ (Supplementary Fig. 8c, d; Supplementary Data 3). In-situ $\delta^{13}C_{V\text{-}PDB}$ values of carbonates exhibit greater variability, indicating small-scale heterogeneity, ranging from −17.5‰ to −4.6‰ (Supplementary Fig. 9; Supplementary Data 4).

Variations and correlations of elements and isotopes

The $\delta^{56}Fe$ and $\delta^{60}Ni$ values in magnetite exhibit a positive correlation (Fig. 2b, c). Negative correlations were observed between the contents of Ni, Co, Y/Ho, Mn, and both $\delta^{60}Ni$ and $\delta^{56}Fe$ values in the studied magnetite samples (Figs. 3a, b, e, f and 4a–c; Supplementary Fig. 6a). In contrast, the Dy/Yb_{PAAS} ratios display a positive correlation with both $\delta^{60}Ni$ and $\delta^{56}Fe$ values in magnetite (Figs. 3d, 4d). Additionally, an anticorrelation was observed between Zn content and $\delta^{60}Ni$ values in magnetite (Fig. 3c). Nickel exhibits positive correlations with Co, Zn, and Y/Ho (Fig. 3h, i; Supplementary Fig. 6b), but an inverse relationship with Dy/Yb_{PAAS} in magnetite (Fig. 3g). Magnetite from the Tongdao and Xinyu IFs displays significantly higher Ni, Co, and Y/Ho levels (Fig. 5a, b; Supplementary Fig. 7b), but lower Dy/Yb_{PAAS} ratios, $\delta^{56}Fe$, and $\delta^{60}Ni$ values, compared to the Jiangkou and Qidong IFs (Fig. 5c–e). Magnetite from the Xinyu IF exhibits the highest levels of Ni and Co, yet the lowest Dy/Yb_{PAAS} ratios, $\delta^{56}Fe$, and $\delta^{60}Ni$ values, except for a few outliers.

It is noteworthy that nearly half of the analysed magnetite shows high molar Ni/Fe ratios, ranging from above 0.0001 to nearly 0.0006 (Supplementary Fig. 10; Supplementary Data 5). Wherever hematite is present alongside magnetite, the latter exhibits more enrichment in Ni and Co (Fig. 5f, g). Additionally, most magnetite samples have higher Y/Ho ratios and Zn contents than hematite (Supplementary Fig. 7d, e), but lower Dy/Yb_{PAAS} ratios (Fig. 5h). The carbonates typically have elevated Mn contents (Supplementary Fig. 8a, b; Supplementary Data 6), following a trend similar to Ni, Co, and Y/Ho in magnetite, but contrasting with $\delta^{56}Fe$ and $\delta^{60}Ni$ trends in magnetite. Carbonates in the Xinyu IF exhibit the highest MnO contents and the highest corresponding bulk-rock $\delta^{13}C_{V\text{-}PDB}$ values (Supplementary Fig. 8b–d). In-situ $\delta^{13}C_{V\text{-}PDB}$ values of calcite, ankerite, and manganosiderite correlate positively with their respective MnO contents (Supplementary Fig. 11a). Interestingly, an inverse correlation is observed between the

https://doi.org/10.1038/s41467-025-62622-z

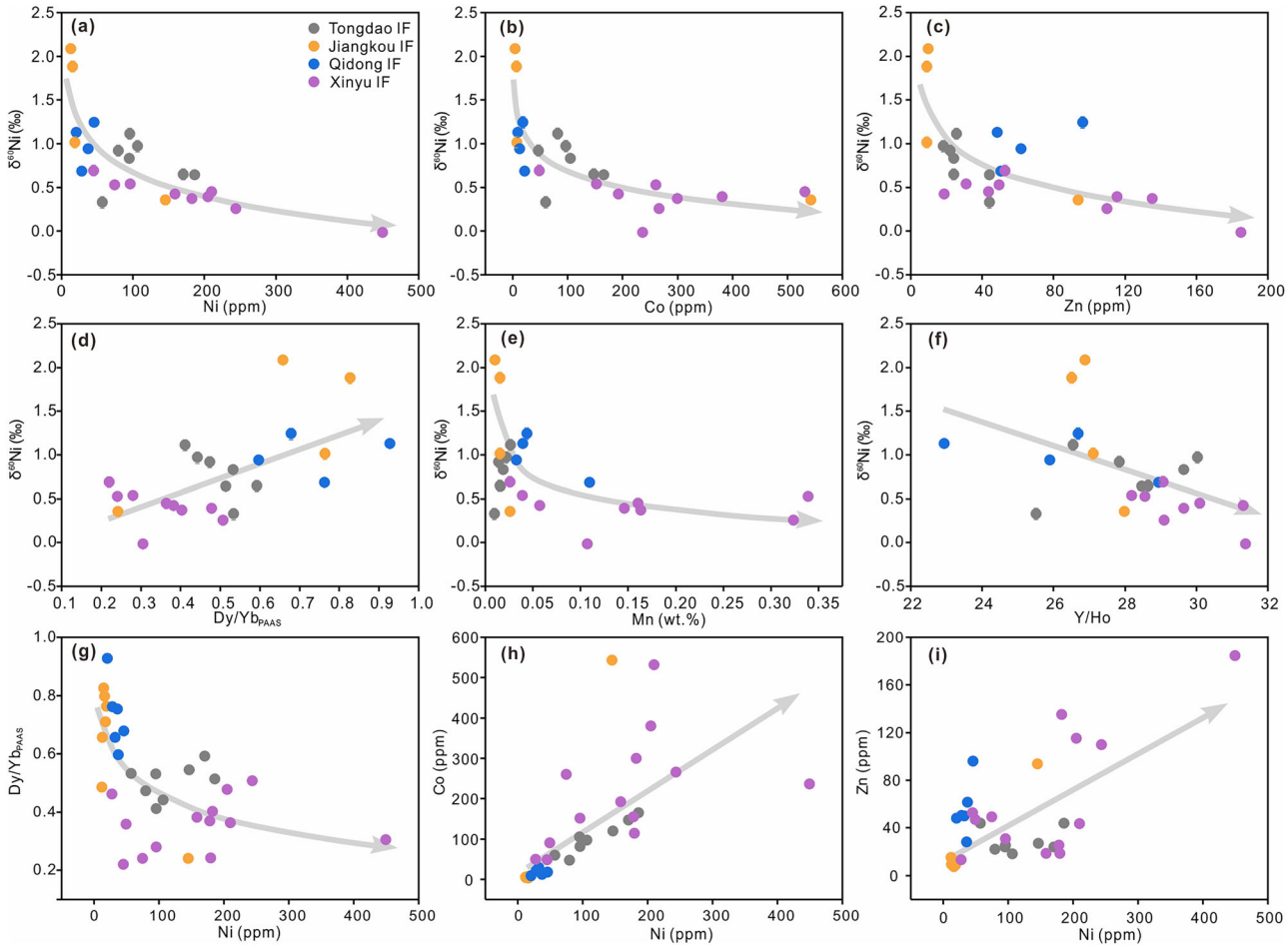

Fig. 3 | Correlations among Ni isotopes, metal elements, and REY patterns in magnetite from the studied Sturtian iron formations. a–**c**, **e**, **f** Cross-plots of Ni, Co, Zn, and Mn contents, as well as Y/Ho ratios, versus δ^{60}Ni, illustrating anticorrelations between these element contents and ratios and the δ^{60}Ni values. **d** Plot of Dy/Yb_{PAAS} versus δ^{60}Ni, demonstrating a positive correlation between Dy/Yb_{PAAS} ratios and δ^{60}Ni values. Here, Dy/Yb_{PAAS} represents the ratio of middle rare earth elements (MREE) to heavy rare earth elements (HREE). Rare earth element data are normalized to post-Archean Australian shale (subscript PAAS). **g** Plot of Ni contents versus Dy/Yb_{PAAS}. An anticorrelation exists between Ni contents and MREE/HREE ratios. **h**, **i** Plots of Ni contents versus Co and Zn contents, showing positive correlations among the variables. Error bars for the δ^{60}Ni data represent two standard deviations (2 SD).

bulk-rock $\delta^{13}C_{V\text{-}PDB}$ values of Mn-rich carbonates and the δ^{60}Ni values of magnetite (Supplementary Fig. 11b, c).

Discussion

The presence of finely-crystalline and platy hematite, characterized by distinct banding and hematite inclusions within ankerite (Supplementary Figs. 2b, f–h, l–n and 3c, e, j), in the Sturtian-aged IFs of the Nanhua Basin suggests its formation through the diagenetic transformation of $Fe(OH)_3$ precursors[22,30,55]. These precursors likely precipitated in the upper water column via oxidation of dissolved Fe^{2+}, subsequently settling on the seafloor as precursor sediments for IFs[18,22] (Fig. 6a, b). Their transformation involved dewatering and silica release (e.g., $2Fe(OH)_3 \rightarrow Fe_2O_3 + 3H_2O$)[16,25], and/or diagenetic replacement of $Fe(OH)_3$[18] within sediment porewater, ultimately forming hematite (Fig. 6b).

Several lines of evidence seemingly suggest that the studied magnetite, ankerite, and manganosiderite originated from in situ DIR and dissimilatory manganese reduction (DMR) of $Fe(OH)_3$ and MnO_2 precursors within sediment porewater during early diagenesis. Here, DIR and DMR are specifically referred to as pathways for Fe and Mn cycling, where microbes utilize organic carbon as an electron donor to reduce Fe^{3+} and Mn^{4+} as terminal electron acceptors, representing potentially ancient respiratory processes[56]. These microbial activities facilitate the release of aqueous Fe^{2+} and Mn^{2+} into anoxic sediment porewater via the following reactions[22,26,28–30] (Eqs. 1 and 2; Fig. 6b, c):

$$CH_3COO^- + 8Fe(OH)_3 \rightarrow 8Fe^{2+} + 2HCO_3^- + 15OH^- + 5H_2O \quad (1)$$

$$CH_3COO^- + 4MnO2 + 3H_2O \rightarrow 4Mn^{2+} + 2HCO_3^- + 7OH^- \quad (2)$$

Subsequently, the reaction between $Fe(OH)_3$ and microbially produced Fe^{2+} facilitated magnetite formation (e.g., $2OH^- + Fe^{2+} + 2Fe(OH)_3 \rightarrow Fe_3O_4 + 4H_2O$)[26,29], while Mn^{2+} – from a precursor MnO_2 phase that also formed in the upper water column – was primarily incorporated into carbonates[57–59].

This interpretation is further supported by petrographic textures and C and Fe isotopic data, which collectively indicate in situ formation of magnetite and Mn-rich carbonates during early diagenesis. First, the magnetite displays euhedral to subhedral morphologies, with sizes ranging from tens to hundreds of microns, and is located within hematite-rich bands (Supplementary Figs. 2f, g, n–p and 3e, j). These bands are oriented parallel to or cross-cutting the layering, consistently aligning with sedimentary bedding, suggesting an authigenic origin for the magnetite. Experimental studies have demonstrated that finely-crystalline magnetite produced through DIR, typically a few hundred nanometers or smaller upon formation, can grow to tens of microns or larger[29]. Second, the occurrence of disseminated, micro-

https://doi.org/10.1038/s41467-025-62622-z

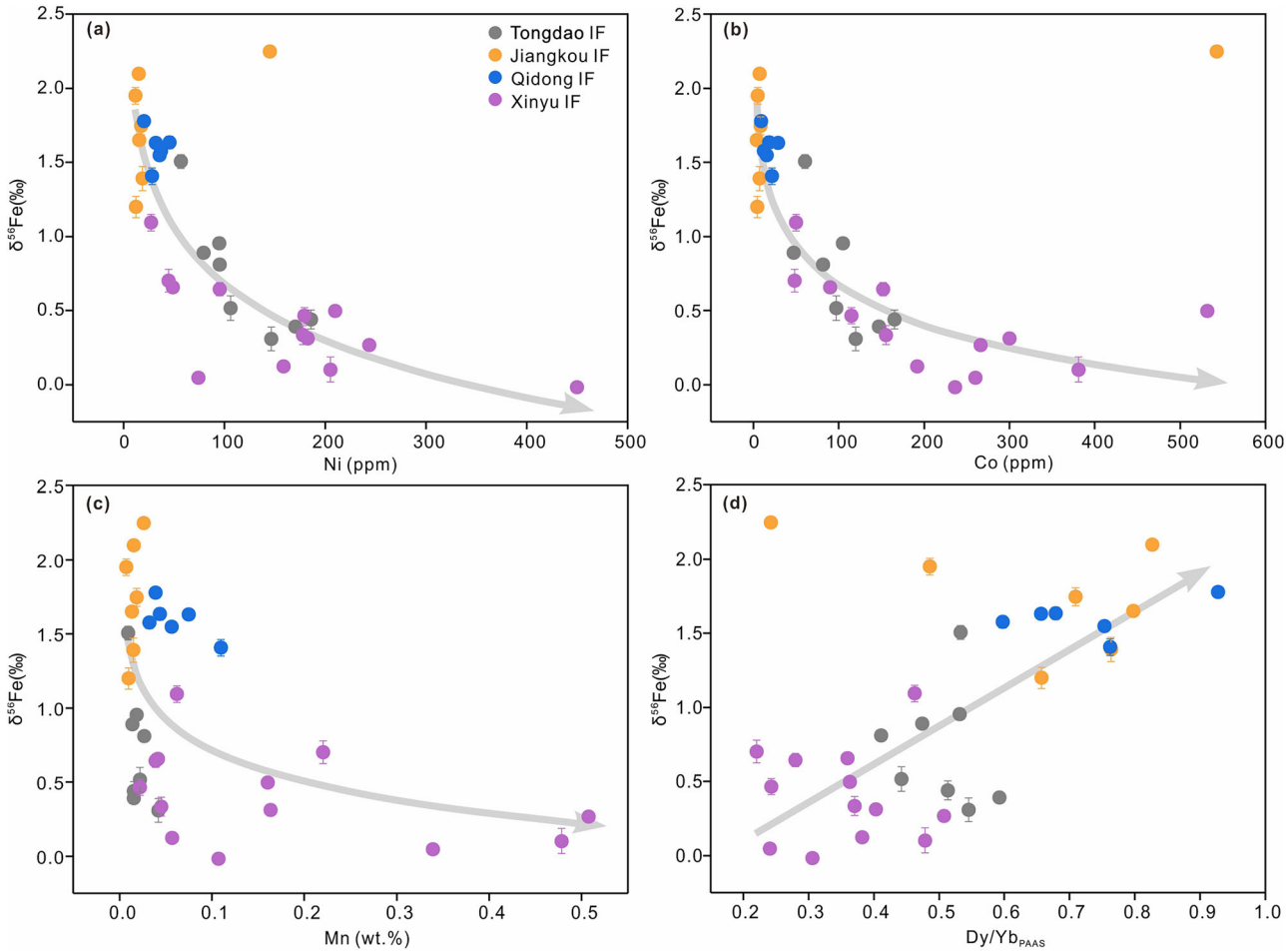

Fig. 4 | Correlations of metal elements and REY patterns with Fe isotope compositions in magnetite from the studied Sturtian iron formations. a–c Plots of Ni, Co, Mn contents versus δ^{56}Fe values, illustrating anticorrelations between the parameters and δ^{56}Fe values. **d** Plot of Dy/Yb_{PAAS} ratios versus δ^{56}Fe values. A positive correlation exists between the ratios of MREE to HREE and δ^{56}Fe values. Error bars for the δ^{56}Fe data represent two standard deviations (2 SD).

sized hematite inclusions within euhedral Mn-rich ankerite rhomboids (Supplementary Fig. 2h) likely reflects in-situ DIR and DMR during the early stage of IF formation[28]. The studied Mn-rich carbonates exhibit low $\delta^{13}C_{V\text{-}PDB}$ values, ranging from −17.5‰ to −4.6‰. These values have traditionally been attributed to mixing of dissolved inorganic carbon (DIC) ($\delta^{13}C_{V\text{-}PDB}$ = ca. 0‰) with remineralized organic carbon, which typically has $\delta^{13}C_{V\text{-}PDB}$ values of ca. −20‰ to −30‰[22,28]. Third, the consistent Fe isotopic signatures of coexisting hematite and magnetite suggest a common precursor. During early diagenesis, $Fe(OH)_3$ transforms into hematite within the sediments while retaining its original δ^{56}Fe values. In the $\delta^{56}Fe_{Hematite} - \delta^{56}Fe_{Magnetite}$ diagram[30] (Fig. 2a), it is evident that magnetite and hematite did not achieve Fe isotopic equilibrium. However, the δ^{56}Fe values of magnetite exhibit a strong positive correlation with those of co-existing hematite, aligning along a 1:1 line (Fig. 2a). This relationship indicates that the synthesis of magnetite by the reaction between hydrothermal Fe^{2+} and $Fe(OH)_3$ is unlikely, as this scenario would be expected to plot along a line with a slope of two-third in Fig. 2a, where one-third of Fe in magnetite would come from hydrothermal sources ($\delta^{56}Fe = 0‰$). The most parsimonious explanation is that magnetite formed in the sediments via in-situ DIR of $Fe(OH)_3$ precursors, predominantly inheriting the Fe isotope composition of the original $Fe(OH)_3$[27,30]. The pronounced Mn enrichment in ^{13}C-depleted authigenic carbonates likely indicates the DMR in the Sturtian-aged IFs of the Nanhua Basin[38,57–60].

Nevertheless, some geochemical features observed in the studied magnetite and Mn-rich carbonates cannot be explained by DIR and DMR alone, suggesting the involvement of additional processes. In particular, DIR and DMR processes fail to account for the considerable variability in δ^{60}Ni values (which can drop to −0.01‰), the inverse relationships between Ni, Co, Zn, Mn and δ^{60}Ni values, the inverse correlation between Ni and Dy/Yb_{PAAS}, and the positive correlation between Dy/Yb_{PAAS} and δ^{60}Ni values in the studied magnetite (Figs. 2b, c, 3a–g and 5d). Additionally, they cannot adequately explain the positive correlation between the in-situ $\delta^{13}C_{V\text{-}PDB}$ values and MnO contents in carbonates (Supplementary Fig. 11a), nor the inverse correlation between bulk-rock $\delta^{13}C_{V\text{-}PDB}$ values of Mn-rich carbonates and magnetite δ^{60}Ni values (Supplementary Fig. 11b, c).

Recent studies have highlighted the role of Fe- and Mn-dependent AOM in driving the formation of authigenic minerals in ferruginous and methanic sedimentary environments. Authigenic magnetite, coexisting with $Fe(OH)_3$ and authigenic carbonates, has been increasingly identified in Fe-rich marine sediments characterized by high CH_4 fluxes at CH_4 seeps[61,62]. The spatial association between methanogens and magnetite indicates that methanogenic archaea mediate Fe reduction, promoting magnetite formation[61,62]. $Fe(OH)_3$ reduction coupled to AOM has also been observed in the methanic zone of ferruginous modern marine sediments, lacustrine environments, and culture-based experiments[26,34,40,46,62,63]. Furthermore, methanogens in the sediments of the methanic zone have been identified as key catalysts for in-situ Fe-driven AOM, highlighting their crucial role in this geochemical process[63–65]. These findings contribute to the understanding of magnetite formation mechanisms in Fe-rich environments

https://doi.org/10.1038/s41467-025-62622-z

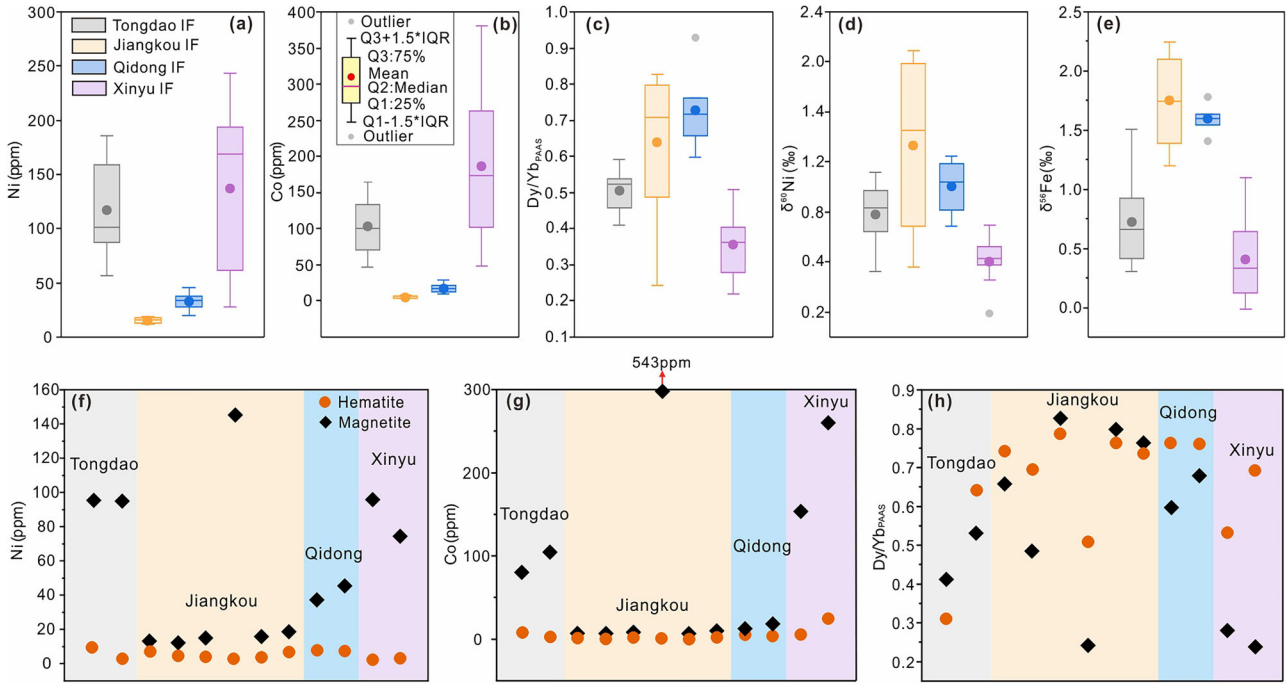

Fig. 5 | Distributions and mineral-specific differences of metal elements, REY patterns and isotope compositions from the studied Sturtian iron formations. **a**–**e** Box plots illustrating the distribution of metal elements, REY, as well as Ni and Fe isotopes in magnetite. **a** Ni contents ($n = 34$), **b** Co contents ($n = 34$), **c** Dy/Yb$_{PAAS}$ ratios ($n = 34$), **d** δ^{60}Ni values ($n = 24$), and **e** δ^{56}Fe values ($n = 34$). Boxes represent the interquartile range (IQR = Q3 − Q1), encompassing the central 50% of the data. The mean is shown as a colored solid circle, and the median (Q2) as a colored solid line within the box. Outliers are indicated by light gray circles. Extreme outliers, defined as exceeding double the IQR from Q2, are excluded from the visualization. **f**–**h** Comparative plots of different IFs were generated to investigate the relationships between Ni (**f**) and Co (**g**) contents, as well as the Dy/Yb$_{PAAS}$ (**h**) ratios in coexisting hematite and magnetite.

and help explain the global increase in Fe^{2+} concentrations in methanic marine sediments[64,66]. Additionally, Mn-dependent AOM is proposed as a major CH_4 sink in CH_4 seep sediments of SO_4^{2-}-depleted early Earth oceans, particularly during the Marinoan deglaciation, facilitating the deposition of Mn-enriched, ^{13}C-depleted carbonates[38,67].

Methanogenesis represents one of the most metal-dependent enzymatic pathways in biology[44]. Nickel, an essential metal in this process, is a crucial component of the porphyrin ring in methyl-coenzyme M reductase (MCR), a key enzyme in methanogenesis, highlighting its unique metal dependence within this enzyme class[48,49,68]. Cobalt is present in cobamides, which play a role in methyl group transfer, while Zn serves as a structural atom in several enzymes[45,69]. AOM by ANME proceeds through a reverse methanogenesis pathway, as ANME possess analogous enzymes to those in the methanogenic pathway[44,45,48,49]. Similar to methanogens, ANME require significant quantities of Ni and Co, with lesser amounts of Zn[42,44]. Furthermore, continental weathering induces Ni isotope fractionation, preferentially releasing isotopically heavier Ni into solution[70]. Consequently, modern global average seawater exhibits relatively heavy Ni isotopic values, with a δ^{60}Ni value of ca. 1.44‰[71,72]. In contrast, both ANME and methanogens preferentially utilize lighter Ni isotopes, fractionating δ^{60}Ni as low as −1.46‰[49,68]. To date, there is no evidence that other types of microbes are capable of substantially fractionating Ni isotopes[5,49,68,69].

The integration of Ni, Co, and REY abundances, along with Ni isotopes, has recently been applied to study CH_4-related biogeochemical cycles. For example, Zhao et al.[5] observed a negative correlation between Ni contents and δ^{60}Ni values, as well as between middle REE (MREE)/HREE ratios and Ni contents in pyrite of the Nantuo Formation, suggesting active methanogenesis during the Marinoan deglaciation. Similarly, Chen et al.[45] suggested that enrichment of Co and Ni, along with low δ^{60}Ni values in pyrite from modern marine sediments, serves as indicator of AOM. Thus, metal-driven AOM likely played a crucial role in transforming $Fe(OH)_3$ and MnO_2 into magnetite and Mn-rich carbonates of the Sturtian-aged IFs examined here. $Fe(OH)_3$ and MnO_2 have been identified as potential electron acceptors for AOM, where diagenesis induced by the upward migration of CH_4 could have occurred through the following reactions[26,38,42,60,67] (Eq. 3 and 4; Fig. 6b, c):

$$CH_4 + 8Fe(OH)_3 + 15H^+ \rightarrow HCO_3^- + 8Fe^{2+} + 21H_2O \quad (3)$$

$$CH_4 + 4MnO_2 + 7H^+ \rightarrow HCO_3^- + 4Mn^{2+} + 5H_2O \quad (4)$$

The low δ^{60}Ni values and enrichment of Ni, Co, and Mn in the analysed magnetite and carbonates may be complicated by abiotic $Fe(OH)_3$ and MnO_2 reduction and dissolution during metal-driven AOM. $Fe(OH)_3$ precipitation has been shown to preferentially incorporate light Ni isotopes and MREE[5,73–75], while MnO_2 serves as an efficient sorbent for Co, Ni, and MREE, with a preference for adsorbing holmium (Ho) over yttrium (Y) from seawater[60]. However, reported Ni isotopic fractionation during $Fe(OH)_3$ uptake typically reaches up to −0.77‰[75]. If this process played a significant role in the present study, the minimum expected δ^{60}Ni values for magnetite would be ca. 0.67‰, which cannot account for the significantly lower δ^{60}Ni values observed in this study. Moreover, the analysed magnetite lacks the characteristic "MREE-bulge" pattern, defined by Dy/Yb$_{PAAS}$ ratios >1, which is typically associated with the reductive dissolution of $Fe(OH)_3$ and MnO_2 and the preferential release of MREE into porewater[60]. Instead, the studied magnetite exhibits relative HREE enrichment over MREE, as reflected in their low Dy/Yb$_{PAAS}$ ratios (Fig. 5c; Supplementary Data 5). Significantly, magnetite typically exhibits lower Dy/Yb$_{PAAS}$ ratios, higher Ni and Co contents, and higher Y/Ho ratios compared to coexisting hematite (Fig. 5f-h; Supplementary Fig. 7e). Furthermore, magnetite and carbonates in the Xinyu IF show the highest Mn

https://doi.org/10.1038/s41467-025-62622-z

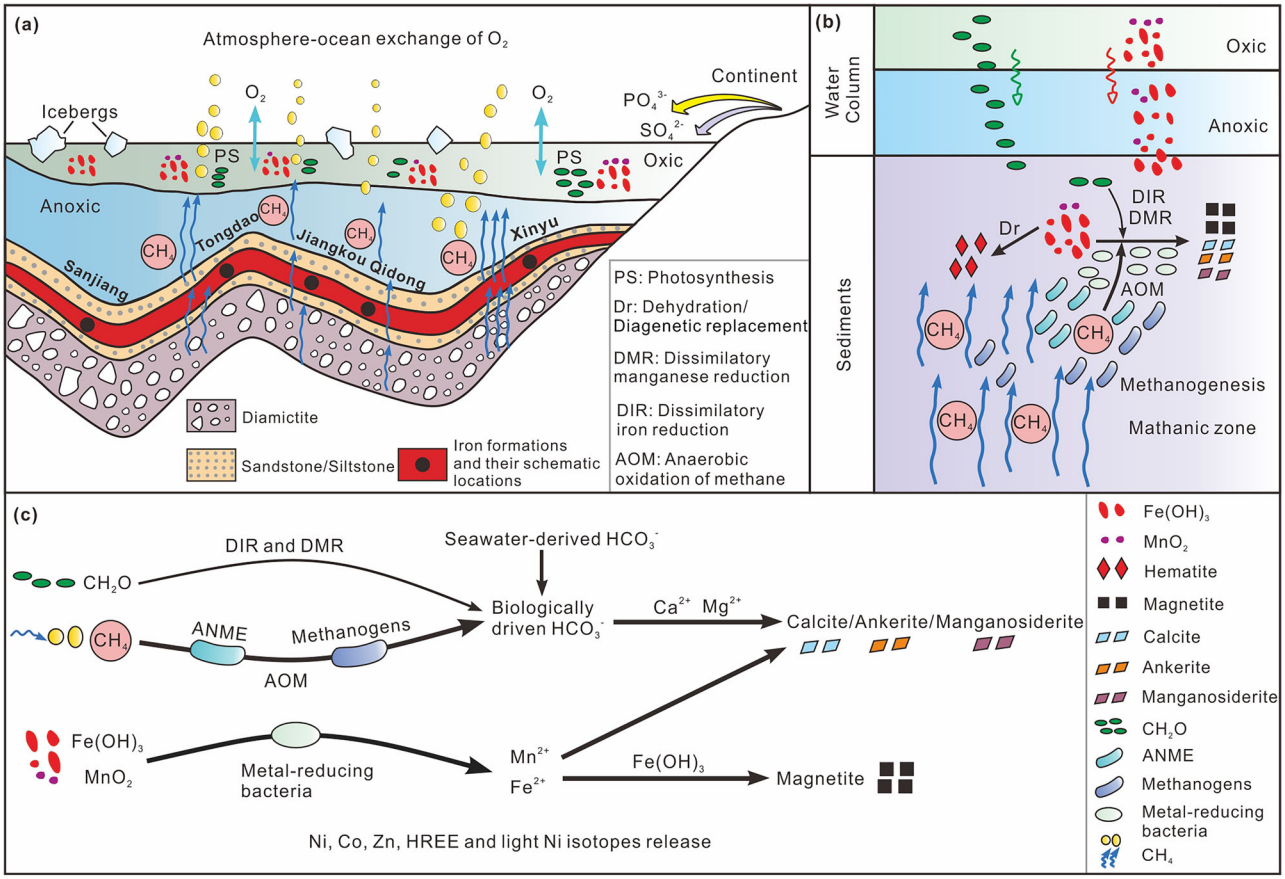

Fig. 6 | Conceptual illustration of biogeochemical cycling during the waning stage of the Sturtian glaciation in the South China Block. a The studied Sturtian-aged IFs were deposited during deglaciation, with minimal glacial influence, allowing for open-water conditions. This created favorable conditions for direct O_2 exchange between the atmosphere and ocean, enhanced nutrient (PO_4^{3-} and SO_4^{2-}) influx from continental weathering, sustained oxygenic photosynthesis and primary productivity recovery, and facilitated ocean stratification, with an anoxic, ferruginous deep layer and an oxygenated surface where the IFs formed. Meanwhile, CH_4 emissions into the atmosphere likely contributed to ice sheet melting or sustained the waning phase between Sturtian glacial episodes. **b**, **c** Under these conditions, metal-driven anaerobic oxidation of methane (AOM), dissimilatory iron reduction (DIR), and dissimilatory manganese reduction (DMR) occurred within anoxic sediment porewater (Eqs. 1–4). These processes involved the reduction of $Fe(OH)_3$ and MnO_2 formed in the upper oxic water column, coupled with varying degrees of methanogens and anaerobic methane-oxidizing archaea (ANME) activity, as well as organic matter oxidation, syntrophic interactions with dissimilatory Fe^{3+} and Mn^{4+}-reducing bacteria, leading to the release of dissolved Fe^{2+} and Mn^{2+} into porewater. Subsequently, the reaction of $Fe(OH)_3$ with Fe^{2+} led to the formation of magnetite. During these processes, ANME and methanogens preferentially absorbed Ni, Co, Zn, HREE, and light Ni isotopes, which were later released into porewater and incorporated into magnetite. Meanwhile, biologically produced HCO_3^- mixed with seawater-derived HCO_3^-, interacting with Ca, Mg, Fe, and Mn cations, led to the formation of ^{13}C-depleted Mn-rich carbonates. The positions of the IFs are schematic. The palaeogeographic framework follows Fig. 1a and reflects previously discussed provisional constraints (see Fig. 1a caption, main text and SI).

enrichment, along with significant HREE enrichment and the highest Y/Ho ratios. Collectively, these observations do not support the release of these elements and isotopes from $Fe(OH)_3$ and MnO_2.

Alternatively, metal-driven AOM in the Sturtian-aged IFs of the Nanhua Basin was due to a complex microbial-mineral interaction network, requiring Fe-reducing microorganisms and reactive $Fe(OH)_3$ and MnO_2 in sediments[34,36,42,46,49,64,66,76,77]. ANME archaea have been recognized as critical microbial agents of metal-driven AOM in the methanic zones of marine sediments[63]. These ANME groups may have contributed to $Fe(OH)_3$ and MnO_2 reduction during CH_4 oxidation, typically engaging in syntrophic interactions with dissimilatory Fe^{3+} and Mn^{4+}-reducing bacteria[34,42,49,77]. Furthermore, methanogens not only produce CH_4 but they play two pivotal roles in sedimentary biogeochemical cycles. First, they can directly reduce $Fe(OH)_3$[76], facilitating a rapid metabolic transition from methanogenesis to $Fe(OH)_3$ reduction[64,66]. Second, methanogens produce intermediate compounds essential for ANME, thus contributing significantly to the AOM process[64,78]. Thus, metal-AOM in this context was likely driven by a diverse microbial community, including ANME, methanogens, and Fe^{3+} and Mn^{4+}-reducing bacteria in anoxic, ferruginous environments[63,64,66]. This is supported by observations of concurrent methanogenesis and metal-driven AOM in active CH_4 seepage areas[42,79].

During metal-driven AOM, varying degrees of ANME and methanogen biomass degradation facilitate the reduction of Fe^{3+} to Fe^{2+} and Mn^{4+} to Mn^{2+}, mobilizing adsorbed Ni, Co, Zn, HREE, and light Ni isotopes into porewater (Fig. 6b, c). Subsequently, the precipitation of authigenic magnetite in sediment porewater incorporates these elements and isotopic signatures, resulting in $\delta^{60}Ni$ values as low as −0.01‰, negative correlations between Ni, Co, Zn, Mn contents and $\delta^{60}Ni$ values, and a positive correlation between Dy/Yb_{PAAS} ratios and $\delta^{60}Ni$ values in the studied magnetite. Additionally, Mn^{2+} was primarily incorporated into the analysed ^{13}C-depleted authigenic carbonates through microbial MnO_2 reduction. These Mn-enriched carbonates, with MnO contents ranging from 0.25 wt.% to 21.48 wt.%, exhibit a wide range of $\delta^{13}C_{V\text{-}PDB}$ values from −17.5‰ to −4.6‰. These C isotope signals are considered to reflect a mixing of multiple DIC sources, including seawater DIC ($\delta^{13}C_{V\text{-}PDB}$ = ca. 0‰), AOM-derived DIC ($\delta^{13}C_{V\text{-}PDB}$ = ca. −60‰), and residual DIC pool in methanogenic zones, which can exhibit extreme ^{13}C-enrichment (up to 50‰ to 70‰) due to CO_2 fractionation during archaeal methanogenesis[28,67,79–82]. Despite the

generally low total organic carbon (TOC) contents (<1.0 wt.%) in the Fulu Formation and its equivalents, the contribution of organic matter-derived DIC ($\delta^{13}C_{V\text{-}PDB}$ = −20‰ to −30‰) cannot be entirely ruled out[21,83]. In low SO_4^{2-} anoxic environments, organic matter degradation occurs via microbial methanogenesis, DIR, and DMR, with methanogenesis being roughly three times more prevalent than the latter processes combined[40,44,84]. While the exact proportions are uncertain, these mixed DIC sources likely infiltrated sediment porewater and were incorporated into authigenic carbonates, as supported by the positive correlation between in-situ $\delta^{13}C_{V\text{-}PDB}$ values and MnO contents in carbonates and the inverse correlation between magnetite δ^{60}Ni values and bulk-rock $\delta^{13}C_{V\text{-}PDB}$ values of carbonates.

Our findings indicate that CH_4-related process played significant role in the precipitation of Sturtian-aged IFs in the Nanhua Basin. However, spatial heterogeneity in CH_4 distribution and the intensity of metal-driven AOM activity likely varied significantly across different IF sites. These variations are thought to be significantly influenced by the bioavailability of Ni, Co, and Zn[44]. Accordingly, the Xinyu IF likely exhibited the highest CH_4 levels and most extensive AOM activity, followed by the Tongdao IF. In contrast, the Jiangkou and Qidong IFs appear to have experienced lower CH_4 levels and weaker AOM. This is supported by the highest Ni and Co contents, along with the lowest Dy/Yb_{PAAS} ratios and δ^{60}Ni values observed within the Xinyu IF, an intermediate status in the Tongdao IF, and contrasting patterns in the Jiangkou and Qidong IFs (Figs. 3 and 5a–d). While no clear trend is observed for Zn, it is most abundant in the Xinyu IF (Supplementary Fig. 7a). At Xinyu, the most extensive CH_4-related activity explains the highest $\delta^{13}C_{V\text{-}PDB}$ values and Mn contents in carbonates, along with the lowest δ^{60}Ni values in magnetite. This correlation arises as methanogenesis can enrich the DIC pool in $\delta^{13}C$[79,80]. However, the lack of magnetite and carbonates in the Sanjing IF suggests that CH_4-related processes, along with DIR and DMR, were either absent or insignificant.

Despite spatial heterogeneity, methanogenesis was active in the Nanhua Basin during the Sturtian period. Sedimentological and geochemical evidence indicates that the studied IFs were deposited during deglaciation (SI). Given CH_4's potent greenhouse properties, a key question is whether it contributed to deglaciation—a possibility that hinges on two critical factors.

First, was CH_4 sufficiently abundant to influence climate? Mass-balance models of global negative $\delta^{13}C$ excursions indicate that CH_4 hydrate reservoirs, and their destabilization, were more extensive during the Neoproterozoic than at any other time in Earth's history[11,12], potentially acting as positive feedback during Marinoan deglaciation[5,11,12]. Although direct estimates of CH_4 fluxes during the Sturtian deglaciation are lacking, elevated molar Ni/Fe ratios in magnetite—nearly half of which exceed 0.0001 and peaking at ~0.0006 (Supplementary Fig. 10; Supplementary Data 5)—suggest enhanced biogenic CH_4 production, comparable to levels inferred for Archean IFs[85]. Consistent with this, the Precambrian ocean-atmosphere system is widely considered to have contained much higher CH_4 levels than present[33–35,38,82]. Furthermore, high CH_4 fluxes are also required to sustain metal-driven AOM in CH_4-rich marine sediments, where the availability of terminal electron acceptors such as $Fe(OH)_3$ and MnO_2 is relatively limited[34,61–63].

Second, could sufficient CH_4 have bypassed oxidation to reach the atmosphere? In CH_4-rich marine sediments, metal-driven AOM oxidizes CH_4 at only ~2% the rate of sulfate-driven AOM[34,63]. Nevertheless, even today—where sulfate-driven AOM dominates—between 6 and 12 Tg/yr of CH_4 escapes to the atmosphere, accounting for 1–10% of natural emissions[13,86]. Given the inherently low oxidation efficiency of metal-driven AOM and abundant coexisting hematite and magnetite in the studied IFs, it is plausible that a significant fraction of CH_4 reached the atmosphere. If marine CH_4 levels were indeed elevated during the Neoproterozoic, such emissions could have contributed to ice sheet melting or sustained the waning phase between Sturtian glacial episodes.

Our geological and geochemical analyses further substantiate the intricate links between CH_4-related processes, Sturtian deglaciation, and Neoproterozoic environmental changes. Our Fe isotope data suggest that the studied Sturtian-aged IFs formed in a stratified ocean, characterized by an anoxic, ferruginous deep layer beneath an oxygenated surface (Fig. 6a; SI). The δ^{56}Fe trends in hematite and magnetite reflect variable Fe^{2+} oxidation, suggesting spatially heterogeneous seawater redox conditions (SI). The exceptionally low δ^{56}Fe values— approaching zero in the Xinyu IF—point to extensive Fe^{2+} oxidation under relatively more oxidizing conditions (SI). The studied magnetite exhibits a positive correlation between δ^{60}Ni, Dy/Yb_{PAAS}, and δ^{56}Fe values, while Co, Ni, and Mn contents show an inverse relationship with δ^{56}Fe values (Figs. 2b, c, 4). Notably, the Xinyu magnetite shows the lowest δ^{60}Ni, Dy/Yb_{PAAS}, and δ^{56}Fe values, along with the highest Co, Ni, and Mn contents. These geochemical patterns suggest a strong interplay between intense methanogenesis, metal-driven AOM, and elevated O_2 levels in shallow seawater. It has been proposed that the O_2 in shallow seawater during the Sturtian glaciation, responsible for oxidizing Fe^{2+} to Fe^{3+}, may have originated from subglacial meltwater O_2 supply[4] or vertical transport processes within glacial ice[87]. However, during Sturtian deglaciation, minimal glacial influence allowed open-water conditions, at least in the Nanhua Basin, enabling direct O_2 exchange between the atmosphere and ocean (Fig. 6a). This shift is supported by evidence of enhanced continental weathering and an active hydrological cycle, as indicated by high Chemical Index of Alteration (CIA) values (65–75), consistently positive δ^{53}Cr (0.64–1.22‰), and elevated aluminosilicate contents in the Nanhua Basin IFs[16,20,88]. The impact of continental weathering was particularly pronounced at Xinyu, as indicated by the highest Mn contents in magnetite and carbonates, significant pyrite abundance originating from bacterial SO_4^{2-} reduction associated with organic matter decomposition[52], and the highest magnetite-to-hematite ratio among the five studied IFs. This is likely due to Xinyu's palaeogeographic proximity to the continental margin, which facilitated the accumulation of weathering products. Along with the widespread abundance of euhedral to subhedral apatite in the sedimentary layers of the Tongdao, Jiangkou, Qidong, and Xinyu IFs (Supplementary Figs. 2h–j, p, 3d, l, m), these features suggest an enhanced influx of continental weathering-derived PO_4^{3-} and SO_4^{2-} into seawater. These nutrients likely fostered favorable conditions for photosynthetic organisms, supporting primary productivity recovery and O_2 production[3,5,6] (Fig. 6a). Notably, PO_4^{3-} is widely recognized as the primary limiting nutrient controlling marine primary productivity over extended geological periods[89]. Further supporting evidence for sustained oxygenic photosynthesis comes from the detection of various steranes—biomarkers of photosynthetic eukaryotes—in Sturtian and Marinoan deposits from the Nanhua Basin[90].

In conclusion, our study reveals a CH_4-related biogeochemical mechanism for Fe-bearing mineral transformation in Sturtian-aged IFs. While exact CH_4 fluxes remain uncertain, our findings underscore its complex interplay with glaciation dynamics, palaeoenvironmental shifts, and biospheric evolution during the Sturtian Snowball Earth, highlighting the need for further investigation.

Methods

Sample preparation

The weathered surfaces and obvious later-stage veins of the studied five IFs samples were initially removed, followed by division into three fragments. One fragment was prepared as polished thin section for petrographic analysis, chemical composition determination, and in-situ C isotope analysis of minerals using light microscopy, EPMA (electron probe microanalyzer)-EDS (energy dispersive X-ray spectroscopy), and a RESOlution 193 nm laser ablation system coupled to a Nu

Plasma II MC-ICP-MS. A second fragment was crushed in a stainless-steel mortar and then pulverized in an agate mill to approximately 200 mesh. The resulting powders were then utilized for bulk-rock C and O isotopic analyses. In the third fragment, hematite and magnetite grains were selected. After extraction, grains were rinsed three times with deionized water, crushed into a fine powder using an agate ring mill, and subsequently utilized for analyses of major and trace elements, as well as Fe and Ni isotopic analysis.

Electron microprobe analysis (EPMA) of carbonate minerals

The quantitative analysis of in-situ major elements in carbonate minerals was conducted using an electron probe microanalyzer at the Wuhan Sample Solution Analytical Technology Co., Ltd in Wuhan. The analysis was conducted using a JEOL JXA-8230 electron microprobe with a 10μm beam diameter, operated at 15 kV accelerating voltage and 5 nA beam current. Rhodonite, dolomite, and hematite were employed as standards for Mn, Ca, Mg, and Fe, respectively. The detection limit for selected elements was set at 0.01 wt. %.

In-situ C isotopic analyses on carbonates

In-situ C isotopic analyses ($n = 106$) of calcite, ankerite, and manganosiderite were conducted using a RESOlution 193 nm laser ablation system coupled to a Nu Plasma II MC-ICP-MS at the State Key Laboratory of Geological Processes and Mineral Resources (GPMR), China University of Geosciences (Wuhan). The instrumental operating conditions and analytical procedures for in-situ C isotope measurements of calcite, dolomite, and siderite are detailed in Chen et al.[91] and Lu et al.[92,93]. A standard-sample bracketing (SSB) method was used to correct instrumental mass bias, with SXD8 calcite, DOL8 dolomite, and SD-5 siderite serving as external standards for the studied calcite, ankerite, and manganosiderite, respectively. Both samples and standards were ablated using a 193 μm laser beam diameter, an 8–10 Hz repetition rate, and an energy density of 3 J/cm^2. The analytical uncertainty for C isotopes is better than 0.5‰ (2 SD), based on repeated analyses of SXD8 calcite, DOL8 dolomite, and SD-5 siderite[91–93]. For high-Mg calcite, dolomite, and siderite, corrections were applied for critical spectral interferences of Mg^{2+}[93]. Data quality was monitored through repeated analyses of the internal laboratory standards OkA153 calcite, DOL9 dolomite, and SD-1 siderite after every 10 samples, yielding an analytical precision better than 0.5‰ (2 SD). The C isotope data are reported in standard δ-notation as $\delta^{13}C$ values, referenced to Vienna Pee Dee Belemnite (V-PDB).

Bulk-rock C and O isotopic analyses

Thirty-six bulk-rock IF samples were used for C and O isotope analyses. Approximately 1 mg of powder was reacted for more than 72 h at 72 °C with an excess of 100% H_3PO_4 under vacuum conditions. The evolved CO_2 was sampled using a Thermo Finnigan Gas Bench II, and the isotopic ratios were measured using a MAT 253 mass spectrometer at the Beijing GeoAnalysis Technology Co., Ltd in Beijing. The isotopic measurements were calibrated against the Chinese national standards (GBW04405, GBW04406, GBW04416, and GBW04417), with analytical errors of less than 0.10‰ and 0.20‰ for $\delta^{13}C$ and $\delta^{18}O$, respectively. The C and O isotope data are reported in the standard δ-notation as $\delta^{13}C$ and $\delta^{18}O$ values, referenced to Vienna Pee Dee Belemnite (V-PDB).

Major and trace element analyses of hematite and magnetite

Analyses of major and trace elements were conducted on thirty-four magnetite and seventeen hematite samples at Qingdao Sparta Analysis & Test Co., Ltd in Qingdao. Major element concentrations were determined using a Thermo Fisher Scientific iCAP 6300 inductively coupled plasma optical emission spectrometer (ICP-OES). Trace elements such as Ni, Co, Zn, rare earth elements and yttrium (REY) were analyzed using inductively coupled plasma mass spectrometry (ICP-MS) with a Thermo Fisher Scientific iCAP RQ instrument. The dissolution procedure was as follows: ~0.04 g of powdered sample was digested in a sealed Teflon beaker with 1.5 ml HF and 1.5 ml of a mixed acid solution of HNO_3 and HCl in a 1:3 (v/v) ratio. The mixture was heated at 180 °C in an electric oven for ~12 h. After cooling, the solution was evaporated to incipient dryness on a hot plate at 150 °C. Subsequently, 1 ml of HNO_3 and 3 ml of H_2O were added, and the sample was further digested in a sealed beaker at 180 °C for ~5 h. Analysis of major and trace elements utilized internal calibrations against reference materials (GBW07315, GBW07316, BHVO-2, and BCR-2).

Fe isotope analysis of hematite and magnetite

Iron isotope ratios of twenty-six magnetite and twenty-two hematite samples were analyzed using a Neptune Plus Multi-Collector Inductively Coupled Plasma Mass Spectrometer (MC-ICP-MS) at the Key Laboratory of Submarine Geosciences and Prospecting Techniques, Ocean University of China, Qingdao. The details of sample dissolution, column chemistry, and instrumental analysis can be found in the works of Dauphas et al.[94], Chen et al.[95] and Li et al.[96]. Following complete dissolution, the solution was evaporated to dryness and then fluxed with 6 N HCl for column chromatography. Fe was purified using 1 ml of pre-cleaned and 6 N HCl-conditioned AG1-X8 resin (a Bio-Rad anion resin), with elution of Fe performed using 0.4 N HCl after a 10 ml 6 N HCl wash[95]. The Fe solutions were diluted with 2% HNO_3 to a concentration of 2 ppm and bracketed with 2 ppm IRMM14. The associated error for each datum is 2 standard deviations (2 SD), with a long-term external precision of ± 0.06‰ for $\delta^{56}Fe$. In this study, Fe isotopes were analyzed in geological reference materials, including the basalt standard JB-2 (0.09 ± 0.02‰) and andesite standard JA-2 (0.14 ± 0.04‰). The $\delta^{56}Fe$ values for all reference materials agree with published data[97]. Fe isotope compositions of the remaining eight magnetite and three hematite samples were analyzed using a Neptune Plus MC-ICP-MS at Wuhan Center, China Geological Survey. The analytical procedures are detailed in Sossi et al.[98] and Hu et al.[99]. Fe was separated using Bio-Rad AG-MP-1M strong anion exchange resin with a recovery rate exceeding 95%. The long-term external reproducibility (2 SD) of Fe isotope analysis is better than ±0.08‰ for $\delta^{56}Fe$, as demonstrated by repeat analyses of multiple Fe isotope standard solutions. The measured Fe isotope compositions of international basalt standards BCR-2, with a $\delta^{56}Fe$ of 0.04 ± 0.03‰, and BHVO-2, with a $\delta^{56}Fe$ of 0.13 ± 0.06‰, are in line with recommended values, considering analytical uncertainties[97,100]. Fe isotope compositions are reported using conventional delta notation relative to the IRMM-14 standard: $\delta^{56}Fe$ (‰) = $[(^{56}Fe/^{54}Fe)_{sample}/(^{56}Fe/^{54}Fe)_{IRMM\text{-}014} - 1] \times 1000$.

Ni isotopic analysis of magnetite

Nickel isotopic analyses were conducted on twenty-four magnetite samples at the Isotope Geochemistry Laboratory of China University of Geosciences, Beijing. Around 5–100 mg of magnetite powders were digested using a concentrated mixture of HF-HNO_3-HCl acid to ensure full dissolution. Aliquots of sample solutions containing 500–800 ng Ni were spiked with a ^{61}Ni – ^{62}Ni double spike to reach an optimal spike-sample ratio of 64:36. The mixtures were subsequently refluxed on hotplates to guarantee sample-spike equilibration prior to column chemistry. Nickel separation from matrices was successfully accomplished through a four-stage chromatography procedure[101–103]. Briefly, the first column used AG1-X8 resin in a media of 6 M HCl to separate Ni from Fe and other matrix elements. The second column applies a mixture of 15 vol.% 10 M HCl and 85 vol.% acetic acid using cation exchange resin Bio-Rad AG50W-X8 to separate Ni from elements such as Mg, Al, Ca, and Ti. In the third separation step, a column was packed with 0.4 ml of AG1-X8 anion exchange resin (Bio-Rad Laboratories, 200 – 400 mesh size) to separate Ni from Na, K, Mn, Cr, V, and other matrix elements[103]. Finally, the first separation step is repeated to further purity the sample if necessary. The total column procedural blank for

Ni was <3 ng, which is negligible compared to 500–800 ng Ni from samples that were processed through the columns.

Nickel isotopic data were determined on a Thermo Scientific® Neptune Plus MC-ICP-MS in medium resolution mode with an Aridus II introduction system. The Neptune MC-ICP-MS was operated under a medium mass resolution mode to separate polyatomic interferences such as $^{40}Ar^{18}O^+$ and $^{40}Ar^{17}OH^+$ on ^{58}Ni. The four Ni isotopes (^{62}Ni, ^{61}Ni, ^{60}Ni, ^{58}Ni) together with ^{57}Fe were measured simultaneously on separate Faraday cups (H2, H1, Axial, L1, and L3). The measurement of ^{57}Fe was used to correct for interference from ^{58}Fe on ^{58}Ni. No detectable peak for polyatomic interferences such as $^{40}Ar^{18}O^+$ and $^{40}Ar^{17}OH^+$ was observable on masses 58 or 57. The background Ni signal for ^{60}Ni was $<10^{-3}$ V, which is negligible relative to the sample signals of ~7–8 V (for 100 ppb solutions). Each sample analysis was bracketed by measurements of a double-spiked NIST SRM 986 nickel solution at similar concentration. The raw data were processed using double-spike equations to correct for isotope fractionation resulting from instrument-induced mass bias and imperfect column yields. The Ni isotopic ratio is presented in the delta (δ) notation as per mil deviation (‰) relative to SRM 986: $\delta^{60}/^{58}Ni$ (‰) = $(^{60}Ni/^{58}Ni)_{sample}/(^{60}Ni/^{58}Ni)_{SRM\text{-}986} - 1$. When processed alongside the samples, reference materials NOD-A-1 and NOD-P-1 yield $\delta^{60}Ni$ values averaging +1.06 ± 0.04‰ (n = 9; 2 SD) and +0.34 ± 0.06‰ (n = 9; 2 SD), respectively, consistent with data from previous studies[70,71,104,105]. During the course of this study, the external precision, as determined by replicate analyses of the reference materials, was better than 0.06‰ (2 SD).

Data availability

The data supporting the findings of this study have been deposited in the Figshare repository (https://doi.org/10.6084/m9.figshare.29648285). Source data are provided with this paper.

References

1. Hoffman, P. F. et al. Snowball Earth climate dynamics and Cryogenian geology-geobiology. *Sci. Adv.* **3**, e1600983 (2017).
2. Sun, R., Grasby, S. E., Shen, J., Xiao, J. & Yin, R. Climate/ocean dynamics and possible atmospheric mercury depletion events during the Late Sturtian deglaciation. *Chem. Geol.* **598**, 120830 (2022).
3. Li, M. et al. Deglacial volcanism and reoxygenation in the aftermath of the Sturtian Snowball Earth. *Sci. Adv.* **9**, eadh9502 (2023).
4. Lechte, M. A. et al. Subglacial meltwater supported aerobic marine habitats during Snowball Earth. *Proc. Natl. Acad. Sci. USA* **116**, 25478–25483 (2019).
5. Zhao, Z. et al. Active methanogenesis during the melting of Marinoan snowball Earth. *Nat. Commun.* **12**, 955 (2021).
6. Bowyer, F. T. et al. Biological diversification linked to environmental stabilization following the Sturtian Snowball glaciation. *Sci. Adv.* **9**, eadf9999 (2023).
7. Song, H. et al. Mid-latitudinal habitable environment for marine eukaryotes during the waning stage of the Marinoan snowball glaciation. *Nat. Commun.* **14**, 1564 (2023).
8. Shen, W., Zhu, X., Li, J. & Yan, B. Mechanism of organic matter accumulation in black shale of the Datangpo Formation: Insights from paleo-environmental variation during the Cryogenian non-glaciation. *Precambrian Res.* **383**, 106889 (2022).
9. Tang, Q. et al. Quantifying the global biodiversity of Proterozoic eukaryotes. *Science* **386**, eadm9137 (2024).
10. Hyde, W. T., Crowley, T. J., Baum, S. K. & Peltier, W. R. Neoproterozoic 'snowball Earth' simulations with a coupled climate/ice-sheet model. *Nature* **405**, 425–429 (2000).
11. Kennedy, M. J., Christie-Blick, N. & Sohl, L. E. Are Proterozoic cap carbonates and isotopic excursions a record of gas hydrate destabilization following Earth's coldest intervals?. *Geology* **29**, 443–446 (2001).
12. Jiang, G., Kennedy, M. J. & Christie-Blick, N. Stable isotopic evidence for methane seeps in Neoproterozoic postglacial cap carbonates. *Nature* **426**, 822–826 (2003).
13. Mao, S. H., Montgomery, A. et al. Aerobic oxidation of methane significantly reduces global diffusive methane emissions from shallow marine waters. *Nat. Commun.* **13**, 7309 (2022).
14. Cox, G. M. et al. Neoproterozoic iron formation: An evaluation of its temporal, environmental and tectonic significance. *Chem. Geol.* **362**, 232–249 (2013).
15. Halverson, G. P. et al. Fe isotope and trace element geochemistry of the Neoproterozoic syn-glacial Rapitan iron formation. *Earth Planet. Sci. Lett.* **309**, 100–112 (2011).
16. Ye, H. et al. Deposition and termination of Neoproterozoic iron formations (NIFs): new insights from NIFs in China. *Earth Sci. Rev.* **256**, 104861 (2024).
17. Lechte, M. A., Wallace, M. W., Hood, A. V. S. & Planavsky, N. Cryogenian iron formations in the glaciogenic Kingston Peak Formation, California. *Precambrian Res.* **310**, 443–462 (2018).
18. Lechte, M. A. & Wallace, M. W. Sedimentary and tectonic history of the Holowilena Ironstone, a Neoproterozoic iron formation in South Australia. *Sediment. Geol.* **329**, 211–224 (2015).
19. Zhang, Q. R., Chu, X. L. & Feng, L. J. Neoproterozoic glacial records in the Yangtze Region, China. *Geol. Soc. London Memoirs* **36**, 357-366 (2011).
20. Wei, W. et al. Redox condition in the Nanhua Basin during the waning of the Sturtian glaciation: a chromium-isotope perspective. *Precambrian Res.* **319**, 198–210 (2018).
21. Zhu, S., Lang, X., Zhao, K. & Hou, M. Influence of turbidity deposition on biogeochemical cycling in sediments and oceanic redox stratification during the waning Sturtian glaciation. *Glob. Planet. Change* **228**, 104184 (2023).
22. Konhauser, K. O. et al. Iron formations: A global record of Neoarchaean to Palaeoproterozoic environmental history. *Earth Sci. Rev.* **172**, 140–177 (2017).
23. Konhauser, K. O., Kappler, A., Lalonde, S. V. & Robbins, L. J. Trace elements in iron formation as a window into biogeochemical evolution accompanying the oxygenation of Earth's atmosphere. *Geosci. Can.* **50**, 239–258 (2023).
24. Köhler, I., Konhauser, K. O., Papineau, D., Bekker, A. & Kappler, A. Biological carbon precursor to diagenetic siderite with spherical structures in iron formations. *Nat. Commun.* **4**, 1741 (2013).
25. Sun, S., Konhauser, K. O., Kappler, A. & Li, Y. L. Primary hematite in Neoarchean to Paleoproterozoic oceans. *Geol. Soc. Am. Bull.* **127**, 850–861 (2015).
26. Konhauser, K. O., Newman, D. K. & Kappler, A. The potential significance of microbial Fe (III) reduction during deposition of Precambrian banded iron formations. *Geobiology* **3**, 167–177 (2005).
27. Johnson, C. M., Beard, B. L., Klein, C., Beukes, N. J. & Roden, E. E. Iron isotopes constrain biologic and abiologic processes in banded iron formation genesis. *Geochim. et. Cosmochim. Acta* **72**, 151–169 (2008).
28. Heimann, A. et al. Fe, C, and O isotope compositions of banded iron formation carbonates demonstrate a major role for dissimilatory iron reduction in ~ 2.5 Ga marine environments. *Earth Planet. Sci. Lett.* **294**, 8–18 (2010).
29. Li, Y. L., Konhauser, K. O., Kappler, A. & Hao, X. L. Experimental low-grade alteration of biogenic magnetite indicates microbial involvement in generation of banded iron formations. *Earth Planet. Sci. Lett.* **361**, 229–237 (2013).
30. Li, W. Q. et al. Contrasting behavior of oxygen and iron isotopes in banded iron formations revealed by in situ isotopic analysis. *Earth Planet. Sci. Lett.* **384**, 132–143 (2013).
31. Milucka, J. et al. Zero-valent sulphur is a key intermediate in marine methane oxidation. *Nature* **491**, 541–546 (2012).

32. Feng, D. et al. A carbonate-based proxy for sulfate-driven anaerobic oxidation of methane. *Geology* **44**, 999–1002 (2016).
33. Fakhraee, M., Hancisse, O., Canfield, D. E., Crowe, S. A. & Katsev, S. Proterozoic seawater sulfate scarcity and the evolution of ocean–atmosphere chemistry. *Nat. Geosci.* **12**, 375–380 (2019).
34. Beal, E. J., House, C. H. & Orphan, V. J. Manganese-and iron-dependent marine methane oxidation. *Science* **325**, 184–187 (2009).
35. Ossa, F. O. et al. Aerobic iron and manganese cycling in a redox-stratified Mesoarchean epicontinental sea. *Earth Planet. Sci. Lett.* **500**, 28–40 (2018).
36. Yan, Z., Joshi, P., Gorski, C. A. & Ferry, J. G. A biochemical framework for anaerobic oxidation of methane driven by Fe (III)-dependent respiration. *Nat. Commun.* **9**, 1642 (2018).
37. Kappler, A. et al. An evolving view on biogeochemical cycling of iron. *Nat. Rev. Microbiol.* **19**, 360–374 (2021).
38. Cai, C. et al. Interlinked marine cycles of methane, manganese, and sulfate in the post-Marinoan Doushantuo cap dolostone. *Geochim. Cosmochim. Acta* **346**, 245–258 (2023).
39. Canfield, D. E. et al. Ferruginous conditions dominated later Neoproterozoic deep-water chemistry. *Science* **321**, 949–952 (2008).
40. Crowe, S. A. et al. The methane cycle in Ferruginous Lake Matano. *Geobiology* **9**, 61–78 (2011).
41. Li, Z. Q. et al. Earth's youngest banded iron formation implies ferruginous conditions in the Early Cambrian ocean. *Sci. Rep.* **8**, 9970 (2018).
42. Yang, H., Yu, S. & Lu, H. Iron-coupled anaerobic oxidation of methane in marine sediments: a review. *J. Mar. Sci. Eng.* **9**, 875 (2021).
43. Liu, L., Guan, H., Xu, L., Sun, Z. & Wu, N. Formation of authigenic carbonates contributed by sulfate-and metal-driven anaerobic oxidation of methane in the northern Okinawa Trough, East China Sea. *Geol. Soc. Am. Bull.* **135**, 1652–1666 (2023).
44. Glass, J. B. & Orphan, V. J. Trace metal requirements for microbial enzymes involved in the production and consumption of methane and nitrous oxide. *Front. Microbiol.* **3**, 61 (2012).
45. Chen, C. et al. Sulfate-driven anaerobic oxidation of methane inferred from trace-element chemistry and nickel isotopes of pyrite. *Geochim. Cosmochim.a Acta* **349**, 81–95 (2023).
46. Ettwig, K. F. et al. Archaea catalyze iron-dependent anaerobic oxidation of methane. *Proc. Natl. Acad. Sci. USA* **113**, 12792–12796 (2016).
47. Zerkle, A. L., House, C. H. & Brantley, S. L. Biogeochemical signatures through time as inferred from whole microbial genomes. *Am. J. Sci.* **305**, 467–502 (2005).
48. Mayr, S. et al. Structure of an F430 variant from archaea associated with anaerobic oxidation of methane. *J. Am. Chem. Soc.* **130**, 10758–10767 (2008).
49. Scheller, S., Goenrich, M., Boecher, R., Thauer, R. K. & Jaun, B. The key nickel enzyme of methanogenesis catalyses the anaerobic oxidation of methane. *Nature* **465**, 606–608 (2010).
50. Lan, Z. W. Research progress on the chronostratigraphic study of Nanhua System in South China. *Sediment. Geol. Tethyan Geol.* **43**, 180–187 (2023).
51. Lin, S. J. et al. Re-division about Fulu Formation and Fulu interglacial epoch in Hunan-Guizhou-Guangxi border area in South China. *Geol. Bull. China* **29**, 195–204 (2010).
52. Wu, C. et al. Termination of Cryogenian ironstone deposition by deep ocean euxinia. *Geochem. Perspect. Lett.* **15**, 1–5 (2020).
53. Tang, J. F., Fu, H. & Yu, Z. Stratigraphy, type and formation conditions of the Late Precambrian banded iron ores in South China. *Chin. J. Geochem.* **6**, 331–341 (1987).
54. Jiang, G., Shi, X., Zhang, S., Wang, Y. & Xiao, S. Stratigraphy and paleogeography of the Ediacaran Doushantuo Formation (ca. 635–551 Ma) in South China. *Gondwana Res.* **19**, 831–849 (2011).
55. Li, Y. et al. Cyanobacteria-ferrihydrite aggregates, BIF sedimentation and implications for Archaean-Palaeoproterozoic seawater geochemistry. *South Afr. J. Geol.* **127**, 359–378 (2024).
56. Konhauser, K. O. Introduction to geomicrobiology. 425 pp. (Blackwell Publishing, 2007).
57. Wei, W. et al. A new salinity-based model for Cryogenian Mn-carbonate deposits. *Precambrian Res.* **403**, 107309 (2024).
58. Zhang, B. et al. Manganese cycling driven by fluctuating redox chemocline in the Ediacaran ocean. *J. Geophys. Res. Solid Earth* **129**, e2024JB029914 (2024).
59. Zhang, B. et al. The molybdenum cycle in the oxygenated Neoproterozoic ocean was coupled to manganese carbonate mineralization. *Commun. Earth Environ.* **5**, 720 (2024).
60. Smrzka, D. et al. Trace elements in methane-seep carbonates: potentials, limitations, and perspectives. *Earth Sci. Rev.* **208**, 103263 (2020).
61. Lin, Z. et al. A novel authigenic magnetite source for sedimentary magnetization. *Geology* **49**, 360–365 (2021).
62. Lin, Z. et al. Methanogenic Archaea as catalysts for magnetite formation in iron-rich marine sediments. *J. Geophys. Res.: Solid Earth* **129**, e2023JB028312 (2024).
63. Aromokeye, D. A. et al. Rates and microbial players of iron-driven anaerobic oxidation of methane in methanic marine sediments. *Front. Microbiol.* **10**, 3041 (2020).
64. Bar-Or, I. et al. Iron-coupled anaerobic oxidation of methane performed by a mixed bacterial-archaeal community based on poorly reactive minerals. *Environ. Sci. Technol.* **51**, 12293–12301 (2017).
65. Egger, M. et al. Iron oxide reduction in methane-rich deep Baltic Sea sediments. *Geochim. Cosmochim. Acta* **207**, 256–276 (2017).
66. Sivan, O., Shusta, S. S. & Valentine, D. L. Methanogens rapidly transition from methane production to iron reduction. *Geobiology* **14**, 190–203 (2016).
67. Cai, C. et al. Anaerobic oxidation of methane by Mn oxides in sulfate-poor environments. *Geology* **49**, 761–766 (2021).
68. Cameron, V., Vance, D., Archer, C. & House, C. H. A biomarker based on the stable isotopes of nickel. *Proc. Natl. Acad. Sci. USA* **106**, 10944–10948 (2009).
69. Hagemeier, C. H., Kruer, M., Thauer, R. K., Warkentin, E. & Ermler, U. Insight into the mechanism of biological methanol activation based on the crystal structure of the methanol-cobalamin methyltransferase complex. *Proc. Natl. Acad. Sci. USA* **103**, 18917–18922 (2006).
70. Ratié, G. et al. Nickel isotope fractionation during tropical weathering of ultramafic rocks. *Chem. Geol.* **402**, 68–76 (2015).
71. Cameron, V. & Vance, D. Heavy nickel isotope compositions in rivers and the oceans. *Geochim. Cosmochim. Acta* **128**, 195–211 (2014).
72. Archer, C., Vance, D., Milne, A. & Lohan, M. C. The oceanic biogeochemistry of nickel and its isotopes: New data from the South Atlantic and the Southern Ocean biogeochemical divide. *Earth Planet. Sci. Lett.* **535**, 116118 (2020).
73. Wasylenki, L. E., Howe, H. D., Spivak-Birndorf, L. J. & Bish, D. L. Ni isotope fractionation during sorption to ferrihydrite: implications for Ni in banded iron formations. *Chem. Geol.* **400**, 56–64 (2015).
74. Wang, S.-J. & Wasylenki, L. E. Experimental constraints on reconstruction of Archean seawater Ni isotopic composition from banded iron formations. *Geochim. Cosmochim. Acta* **206**, 137–150 (2017).
75. Gueguen, B. et al. Variable Ni isotope fractionation between Fe-oxyhydroxides and implications for the use of Ni isotopes as geochemical tracers. *Chem. Geol.* **481**, 38–52 (2018).

76. Vigderovich, H. et al. Evidence for microbial iron reduction in the methanic sediments of the oligotrophic southeastern Mediterranean continental shelf. *Biogeosciences* **16**, 3165–3181 (2019).
77. Xiao, X. et al. Metal-driven anaerobic oxidation of methane as an important methane sink in methanic cold seep sediments. *Microbiol. Spectr.* **11**, e05337–22 (2023).
78. Zhang, J. et al. Microbial reduction of Fe(III) in illite–smectite minerals by methanogen *Methanosarcina mazei*. *Chem. Geol.* **292**, 35–44 (2012).
79. Sivan, O., Antler, G., Turchyn, A. V., Marlow, J. J. & Orphan, V. J. Iron oxides stimulate sulfate-driven anaerobic methane oxidation in seeps. *Proc. Natl. Acad. Sci. USA* **111**, E4139–E4147 (2014).
80. Peckmann, J. & Thiel, V. Carbon cycling at ancient methane seeps. *Chem. Geol.* **205**, 443–467 (2004).
81. Feng, D. et al. Using *Bathymodiolus* tissue stable carbon, nitrogen and sulfur isotopes to infer biogeochemical processes at a cold seep in the South China Sea. *Deep Sea Res. Part I: Oceanogr. Res. Pap.* **104**, 52–59 (2015).
82. Slotznick, S. P. & Fischer, W. W. Examining Archean methanotrophy. *Earth Planet. Sci. Lett.* **441**, 52–59 (2016).
83. Wang, P. et al. Negative carbon isotope excursions of the Sturtian glacial sediments in the Neoproterozoic Nanhua Basin and their geological significance. *Acta Sedimentol. Sin.* **42**, 2020–2030 (2024).
84. Kuntz, L. B., Laakso, T. A., Schrag, D. P. & Crowe, S. A. Modeling the carbon cycle in Lake Matano. *Geobiology* **13**, 454–461 (2015).
85. Konhauser, K. O. et al. Oceanic nickel depletion and a methanogen famine before the Great Oxidation Event. *Nature* **458**, 750–753 (2009).
86. Lapham, L. L. et al. Methane leakage through the sulfate–methane transition zone of the Baltic seabed. *Nat. Geosci.* **17**, 1277–1283 (2024).
87. Busigny, V. et al. Origin of the Neoproterozoic Fulu iron formation, South China: Insights from iron isotopes and rare earth element patterns. *Geochim. Cosmochim. Acta* **242**, 123–142 (2018).
88. Wu, C. Z. et al. Genesis of the Fulu Cryogenian iron formation in South China: Synglacial or interglacial?. *Precambrian Res.* **376**, 106689 (2022).
89. Guilbaud, R. et al. Phosphorus-limited conditions in the early Neoproterozoic ocean maintained low levels of atmospheric oxygen. *Nat. Geosci.* **13**, 296–301 (2020).
90. Wang, T. G. et al. Organic molecular evidence in the Late Neoproterozoic tillites for a palaeo-oceanic environment during the Snowball Earth era in the Yangtze region, southern China. *Precambrian Res.* **162**, 317–326 (2008).
91. Chen, W., Lu, J., Jiang, S. Y., Zhao, K. D. & Duan, D. F. In situ carbon isotope analysis by laser ablation MC-ICP-MS. *Anal. Chem.* **89**, 13415–13421 (2017).
92. Lu, J. et al. Determination of carbon isotopes in carbonates (calcite, dolomite, magnesite, and siderite) by femtosecond laser ablation multi-collector ICP-MS. *J. Anal. Spectrom.* **37**, 278–288 (2022).
93. Lu, J. et al. In situ carbon isotopic analyses of magnesium-rich carbonates by LA-MC-ICP-MS at low mass resolution using an iterative isobaric interference correction. *Talanta* **285**, 127371 (2025).
94. Dauphas, N. et al. Iron isotopes may reveal the redox conditions of mantle melting from Archean to present. *Earth Planet. Sci. Lett.* **288**, 255–267 (2009).
95. Chen, L. et al. Fe–Mg isotopes trace the mechanism of crustal recycling and arc magmatic processes in the Neo-Tethys subduction zone. *J. Geophys. Res. Solid Earth* **128**, e2023JB026778 (2023).
96. Li, D.-Y. et al. Integrated element doping and standard–sample bracketing for enhanced Fe–Zn isotope precision in MC-ICPMS. *Rapid Commun. Mass Spectrom.* **39**, e10041 (2025).
97. He, Y. et al. High-precision iron isotope analysis of geological reference materials by high-resolution MC-ICP-MS. *Geostand. Geoanaly. Res.* **39**, 341–356 (2015).
98. Sossi, P. A., Halverson, G. P., Nebel, O. & Eggins, S. M. Combined separation of Cu, Fe and Zn from rock matrices and improved analytical protocols for stable isotope determination. *Geostand. Geoanal. Res.* **39**, 129–149 (2015).
99. Hu, J. et al. Trace element and isotope (C, S, Sr, Nd, Fe) geochemistry constraints on the sedimentary environment of the early Neoproterozoic Shilu BIF and associated dolostones, South China. *Precambrian Res.* **372**, 106610 (2022).
100. Craddock, P. R. & Dauphas, N. Iron isotopic compositions of geological reference materials and chondrites. *Geostand. Geoanaly. Res.* **35**, 101–123 (2011).
101. Wang, S.-J., Rudnick, R. L., Gaschnig, R. M., Wang, H. & Wasylenki, L. E. Methanogenesis sustained by sulfide weathering during the Great Oxidation Event. *Nat. Geosci.* **12**, 296–300 (2019).
102. Wang, S.-J., Li, S.-J., Lin, Y. & Sheng, S.-Z. Mass-dependent nickel isotopic variations in achondrites and lunar rocks. *Geochim. Cosmochim. Acta* **350**, 16–27 (2023).
103. Ratnayake, D. M., Tanaka, R. & Nakamura, E. Novel nickel isolation procedure for a wide range of sample matrices without using dimethylglyoxime for isotope measurements using MC-ICP-MS. *Anal. Chim. Acta* **1181**, 338934 (2021).
104. Gall, L. et al. Nickel isotopic compositions of ferromanganese crusts and the constancy of deep ocean inputs and continental weathering effects over the Cenozoic. *Earth Planet. Sci. Lett.* **375**, 148–155 (2013).
105. Gueguen, B., Rouxel, O., Ponzevera, E., Bekker, A. & Fouquet, Y. Nickel isotope variations in terrestrial silicate rocks and geological reference materials measured by MC-ICP-MS. *Geostand. Geoanal. Res.* **37**, 297–317 (2013).
106. Wang, J. et al. Evolution of the South China Paleocontinent and related resource-environmental developments: from Columbia to Gondwana. *Acta Sedimentol. Sin.* **42**, 1849–1875 (2024).
107. Polyakov, V. B., Clayton, R. N., Horita, J. & Mineev, S. D. Equilibrium iron isotope fractionation factors of minerals: Reevaluation from the data of nuclear inelastic resonant X-ray scattering and Mössbauer spectroscopy. *Geochim. Cosmochim. Acta* **71**, 3833–3846 (2007).

Acknowledgements

This research was supported by the National Natural Science Foundation of China (42172079 to J.H., 42121005 to S.Z.L., 41973010 to S.-J.W., 42488201 to W.J.X. and 42475052 to P.L), the National Key R&D Program of China (2023YFC2812904) to J.H., the Taishan Scholar Program (tspd20210305) to S.Z.L., the Fundamental Research Funds for the Central Universities (Grant 2652023001) to S.-J.W., the Taishan Scholar Program (tstp20231214) to S.Y.Y., and the Fundamental Research Funds for the Central Universities (No.202172003) to S.Z.L. We also thank for the technical support of the National Large Scientific and Technological Infrastructure "Earth System Numerical Simulation Facility" (https://cstr.cn/31134.02.EL). Special appreciation is extended to Prof. Paul F. Hoffman, Dr. Lei Liu, Dr. Zhihui An, and Dr. Zhihong Wang for their profound insights and discussions on scientific issues.

Author contributions

J.H., S.Z.L., and S.-J.W. designed the work. J.H., S.Z. L., S.-J.W., K.O.K., J.P., H.X. G., S.-Y. J., W.C., H.C., Z.Q., P.L., Y.H.S. and Z.-X. J. wrote the manuscript, D.Y.L., W.N., S.-Y.J., W.C., H.C., X.H.L., Y.Z., R.R.L., and X.M.Y. analysed and interpreted the data. All authors contributed to discussions.

Competing interests

The authors declare no competing interests.

Additional information

Supplementary information The online version contains supplementary material available at https://doi.org/10.1038/s41467-025-62622-z.

Correspondence and requests for materials should be addressed to Sanzhong Li or Shui-Jiong Wang.

Peer review information *Nature Communications* thanks Ganqing Jiang and the other anonymous reviewer(s) for their contribution to the peer review of this work. A peer review file is available.